How to cite: *Angew. Chem. Int. Ed.* **2025**, e202514410
doi.org/10.1002/anie.202514410

Batteries

Synergistic Regulation of Electrolyte and Electrode Structures Enhance Ammonium Vanadate Mg-storage Performance for 100 mAh-Level Mg-ion Pouch Cells

Fan Qiao[+], Wenwei Zhang[+], Junjun Wang, Jiayi Cheng, Jinghao Li, Lianmeng Cui, Liang Zhou,* and Qinyou An**

Abstract: Aqueous Mg-ion batteries (AMIBs) have attracted increasing interest due to their safety, fast kinetics, and sustainability. However, the development of AMIBs is hindered by the narrow electrochemical stability window (ESW) of electrolytes and electrode degradation. Here, a synergistic strategy, regulating both electrolyte and electrode structures, is proposed to enable high-performance AMIBs. Incorporating a polyethylene glycol crowding agent into $Mg(ClO_4)_2/H_2O$ electrolyte regulates the solvation structure, which suppresses hydrogen evolution, and expands the ESW beyond 3.1 V. Meanwhile, an ammonium vanadate (NHVO) material with enlarged interlayer spacing is synthesized, and a freestanding NHVO/graphene oxide/carbon nanotube (NHVO/GO/CNT) electrode is constructed to enhance Mg^{2+} diffusion and mitigate vanadium dissolution. Under the synergistic regulation, NHVO/GO/CNT exhibits a high capacity of 284.0 mAh g^{-1} and the longest cycling lifespan (16 000 cycles with 95.6% capacity retention). The solvation structure of electrolytes and interfacial stabilization mechanisms are elucidated through theory calculations. The Mg-storage mechanism of NHVO based on a single-phase insertion/extraction reaction with NH_4^+/Mg^{2+} displacement phenomenon is revealed. The constructed multilayer Mg-ion pouch cell achieves a record-high capacity of 103.7 mAh. The integrated solar cell-pouch cell device demonstrates the feasibility of photo-charging AMIBs for the first time. This work offers a viable strategy toward practical, high-performance multivalent-ion batteries.

Introduction

The surge in global energy demand and the scarcity of lithium resources have driven the development of efficient, safe, and sustainable energy storage technologies beyond lithium-ion batteries.[1,2] Among various candidates, multivalent ions (e.g., Zn^{2+}, Mg^{2+}, Ca^{2+}) have emerged as promising charge carriers due to their ability to enable multielectron transfer, offering the potential for high-energy-density storage devices. Mg-ion batteries (MIBs) have attracted significant research interest owing to their low reduction potential (−2.37 V vs. SHE), abundant natural reserves of magnesium, and high volumetric capacity (3833 mAh cm^{-3}, twice that of lithium).[3] However, due to the high charge density of Mg^{2+}, it exhibits high desolvation energy in organic electrolytes and strong Coulombic interactions with host materials.[4] As a result, the mainstream cathode materials for MIBs are still limited to chalcogen compounds, which feature weak binding interactions but low working voltage (below 1.2 V vs. Mg^{2+}/Mg).[5] Furthermore, the high corrosiveness of chloride-containing Mg electrolytes and their poor compatibility with high-voltage oxides or polyanionic salt materials pose significant challenges for developing high-capacity MIBs with practical potential in current systems.[6,7] Therefore, exploring or developing alternative Mg electrochemical systems is of great importance for the long-term advancement of MIBs.

Aqueous Mg-ion batteries (AMIBs), employing water-based electrolytes, present notable advantages, including high ionic conductivity, low desolvation energy, improved safety, and fast ion diffusion kinetics (due to the charge-shielding effect of H_2O molecules).[8] More importantly, AMIBs can achieve working voltage comparable to that of chalcogen-based cathode materials in organic systems.[9] Therefore, AMIBs hold promise to achieve high-performance Mg storage chemistry. Currently, the development of AMIBs faces key challenges such as the narrow electrochemical stability window (ESW) and poor stability of aqueous electrolytes, as well as the dissolution and structural degradation of electrode materials (Figure 1a).[10] These issues lead to traditional AMIBs suffering from low Coulombic efficiency (CE) and poor cycling performance. To address these challenges, researchers have devoted significant efforts to improving the performance of AMIBs. Jin et al. reported a $MgCl_2{\cdot}6H_2O$

---

[*] F. Qiao[+], W. Zhang[+], J. Wang, J. Cheng, J. Li, L. Cui, L. Zhou, Q. An
State Key Laboratory of Advanced Technology for Materials Synthesis and Processing, Wuhan University of Technology, Wuhan 430070, China
E-mail: wjunjun@whut.edu.cn
liangzhou@whut.edu.cn
anqinyou86@whut.edu.cn

L. Zhou, Q. An
Hubei Longzhong Laboratory Wuhan University of Technology (Xiangyang Demonstration Zone) Xiangyang, Hubei 441000, China

[+] Both authors contributed equally to this work.

Additional supporting information can be found online in the Supporting Information section

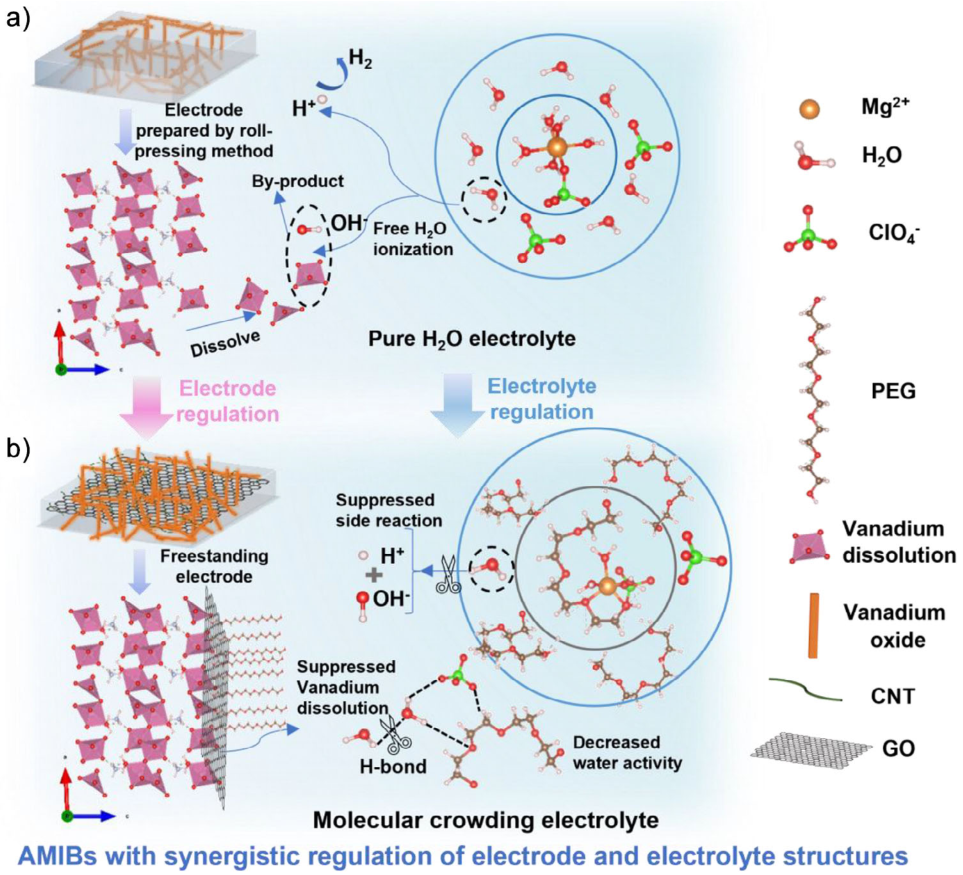

Figure 1. Schematic diagrams of the Mg^{2+} solvation shell and electrochemical behaviors at ammonium vanadate/graphene oxide/carbon nanotube (NHVO/GO/CNT) interface in a) an aqueous Mg electrolyte and b) a polyethylene glycol (PEG) based molecular crowding Mg electrolyte.

hydrated eutectic electrolyte with an ESW exceeding 3.0 V, and the assembled CuHCF||Mn-NVO Mg-ion full cell demonstrated a discharge capacity of 69.1 mAh g^{-1} and stable cycling over 800 cycles.[11] Alshareef et al. demonstrated a PTCDA||CuHCF Mg-ion pouch cell assembled with a $Mg(NO_3)_2{\cdot}6H_2O$-based hydrated eutectic electrolyte, exhibiting a capacity of 10 mAh and 100 cycles.[12] Wei et al. achieved over 100 cycles of stable Mg storage in vanadium oxide materials by pre-insertion chemical regulation of the vanadium oxide material structure[13] or reconstructing the solvation structure of Mg electrolytes.[14] Han et al. achieved a Mg storage lifetime of 1000 cycles for $NaV_8O_{20}{\cdot}nH_2O$ through an ether/water hybrid Mg electrolyte.[15] Mai et al. achieved a cycling stability of 3000 cycles for $VO_2(B)$ through a protons and Mg^{2+} ions co-insertion strategy, and the assembled CuHCF||$VO_2(B)$ Mg-ion pouch cell delivered a capacity of 14 mAh.[16] NuLi et al. assembled a PTCDI||EG Mg-ion full cell using an acetonitrile/water mixed electrolyte and a copper foam-modified separator, which exhibited a life of 600 cycles.[17] Wang et al. reported a PPMDA||$Mg_xLiV_2(PO_4)_3$ full cell that delivered a discharge capacity of 52 mAh g^{-1} in 4 M $Mg(TFSI)_2/H_2O$ electrolyte.[9] In addition, some strategies such as interlayer engineering,[18] vacancy,[19] or ion doping[20] have been employed to enhance the Mg storage performance of electrode materials in aqueous electrolytes. However, despite these efforts, the cycle life of high-capacity inorganic electrode materials in current AMIBs remains below 5000 cycles (Table S1), and the capacity of Mg-ion pouch cells is less than 20 mAh (Table S2), both of which fall far short of the requirements for practical applications. Therefore, developing new strategies to further enhance the Mg storage performance of electrode materials and achieve high-capacity Mg-ion pouch cells is crucial for advancing AMIBs toward real-world applications.

In this work, a synergistic strategy, combining simultaneous regulation of both the electrolyte and electrode structure, is proposed to enhance the electrochemical performance of AMIBs (Figure 1b). Regarding electrolyte regulation, a highly water-soluble and non-toxic PEG molecular crowding agent is introduced into a low-cost $Mg(ClO_4)_2/H_2O$ electrolyte. The addition of PEG confines H_2O molecules within the crowding agent network, weakening the intermolecular hydrogen bonds (HBs) between H_2O molecules while strengthening the intrinsic covalent O-H bonds. This will increase the overpotential for the hydrogen evolution reaction (HER) and broaden the ESW. For electrode structure regulation, a freestanding NHVO/GO/CNT composite anode was constructed. Compared to electrodes obtained through traditional rolling methods, the freestanding NHVO/GO/CNT electrode has higher electron conductivity while inhibiting the dissolution and structural degradation of NHVO. Under the effect of this synergistic regulation, the NHVO/GO/CNT demonstrates an exceptional rate capability of 136.5 mAh g^{-1} at 2.0 A g^{-1} and an ultra-long cycle life of 16000 cycles with 95.6% capacity retention at 1.0 A g^{-1}. In addition, the solvation structure of electrolytes and the stabilization mechanism at the electrode–electrolyte interface were elucidated. The Mg-storage mechanism of NHVO based on a single-phase insertion/extraction reaction, and the displacement phenomenon between Mg^{2+} and NH_4^+ were revealed. The assembled multilayer aqueous Mg-ion pouch cell, using a nickel-based Prussian blue analog (NiHCF) as the cathode, delivered the highest capacity of 103.7 mAh among all reported Mg-ion pouch cells. Furthermore, the integrated solar cell-pouch cell device demonstrated, for the first time, the feasibility of photo-charging AMIBs. These findings provide a novel strategy for achieving high-performance AMIBs through integrating the regulation of electrode and electrolyte structures.

Results and Discussion

A non-toxic PEG ($HO(CH_2CH_2O)_nH$, $M_n = 200$) molecular crowding agent and a low-cost $Mg(ClO_4)_2/H_2O$ electrolyte are selected to prepare molecular crowding Mg electrolytes. As illustrated in Figure S1, a series of low concentration aqueous molecular crowding Mg electrolytes were prepared: 1.0 M $Mg(ClO_4)_2$ in xPEG-(1-x)H_2O (x = 0, 40%, 60%, 80%, and 90%, labeled as pure H_2O, 40% PEG, 60% PEG, 80% PEG, and 90% PEG). Figure 2a displays the electrostatic potential (ESP) mapping of PEG and H_2O. It reveals that the negatively charged ether oxygen (-O-) or hydroxyl oxygen atoms (-OH) in PEG chain can readily form HBs with H_2O molecules. Simultaneously, the high polarity of terminal hydroxyl groups in PEG facilitates adsorption at electrode interfaces. The binding energy results, obtained by density functional theory (DFT) calculations, indicate that PEG exhibits both HBs donor and acceptor properties, preferentially interacting with H_2O. Furthermore, the binding energy between PEG and Mg^{2+} is lower than those of H_2O-H_2O, PEG-H_2O, and H_2O-Mg^{2+} (Figure 2b). Since H_2O is a rigid small molecule while PEG is a flexible long-chain molecule, the PEG chains can rotate or twist when co-ordinating with Mg^{2+} to achieve a more uniform charge distribution (Figures S2 and S3). This allows the PEG-Mg^{2+} complex to exist in a more stable form, which also implies that PEG-Mg^{2+} has a more negative binding energy compared to PEG-H_2O. The binding energy calculation results suggest that the ether groups of PEG molecules may participate in the solvation structure of Mg^{2+}, consequently disrupting the original HBs network. Additionally, PEG boasts a higher the highest occupied molecular orbital (HOMO) energy level and a lower the lowest unoccupied molecular orbital (LUMO) energy level compared to H_2O.[21] This signifies its enhanced ability to donate and accept electrons, suggesting that PEG can strengthen interactions with other species, such as Mg^{2+} and electrode materials (Figure 2c). Molecular dynamics (MD) simulations were further employed to analyze the solvation structure of Mg^{2+} in pure H_2O, 60% PEG and 90% PEG electrolytes (Figures 2d–f and S2–S3). The Radial distribution function (RDF) analyses indicate that as the PEG content increases, the coordination numbers (CNs) of PEG in the primary solvation shell of Mg^{2+} gradually rises from 0 to 3.5 (Figures 2f, S4b, and S5b). Correspondingly, the dominant solvation species of Mg^{2+} ions transition from $[Mg(H_2O)_6]^{2+}$ to $[Mg(ClO_4^-)(H_2O)_3PEG]^+$ and $[Mg(ClO_4^-)_2(H_2O)(PEG)_3]^+$ (Figures 2d, S4c, and S5c). These results demonstrate that, in molecular crowding electrolytes, PEG molecules can participate in the primary solvation shell of Mg^{2+}, effectively displacing active H_2O molecules, thereby suppressing parasitic side reactions at the electrolyte-electrode interface and broadening the ESW. MD simulations additionally revealed differences in the types and proportions of HBs across the three electrolytes (Figure S6). After PEG addition, the number of HB types increased from 2 to 4, and the proportion of H_2O–H_2O HBs decreased significantly from 79.7% to 8%. These results indicate that the introduction of PEG disrupts the HBs network of the pure H_2O electrolyte, which is beneficial for suppressing the activity of H_2O molecules.

The Fourier transform infrared (FTIR) analysis of the different electrolytes revealed that as the PEG content increased from 0% to 90%, both the O-H stretching vibration peak (3200–3400 cm^{-1}) and the H-O-H bending vibration peak (1550–1750 cm^{-1}) for H_2O exhibited blue shifts (Figure 2g), indicating a strengthening of the covalent O-H bonds of H_2O.[15] Raman spectroscopy further corroborated the FTIR findings (Figure S7). ^{1}H nuclear magnetic resonance (NMR) spectra (Figure 2h) of the electrolytes showed that the chemical shift of protons for H_2O decreased progressively as the PEG content increased from 0% to 80%. For the 90% PEG electrolyte, the proton signal intensity became undetectable, which is attributed to the significant reduction in the HBs between H_2O molecules.[22] This indicates that the HBs network present in the pure H_2O electrolyte is disrupted. Moreover, this observation is consistent with the MD simulation results, which show a marked decrease in HBs among H_2O molecules. Linear sweep voltammetry (LSV) tests, performed using a three-electrode configuration with Ti foil as the working electrode, activated carbon cloth (ACC) as the counter electrode, and an Ag/AgCl reference electrode, reveal that the ESW gradually widens as the PEG content increases, reaching over 3.1 V for the 90% PEG electrolyte (Figure S8). This indicates that the introduction of PEG can effectively suppress H_2O decomposition. Ionic conductivity tests of different electrolytes at 25 °C show that, with increasing PEG content, the ionic conductivity decreases from 63.7 mS cm^{-1} to less than 1.0 mS cm^{-1} (Figure S9).

The above results indicate that the addition of the PEG crowding agent effectively enhances the stability of the $Mg(ClO_4)_2/H_2O$ electrolyte, but it also leads to a decrease in ionic conductivity. Therefore, identifying the optimal electrolyte composition that balances the cycling stability and rate performance of electrode materials requires further evaluation through electrochemical testing. NHVO, featuring a large interlayer spacing and high theoretical capacity, was selected as the electrode material. X-ray diffraction (XRD) pattern (Figure 3a) shows that the monoclinic phase NHVO with an 8.3Å large interlayer spacing was successfully prepared (PDF#51-0376). Scanning electron microscopy

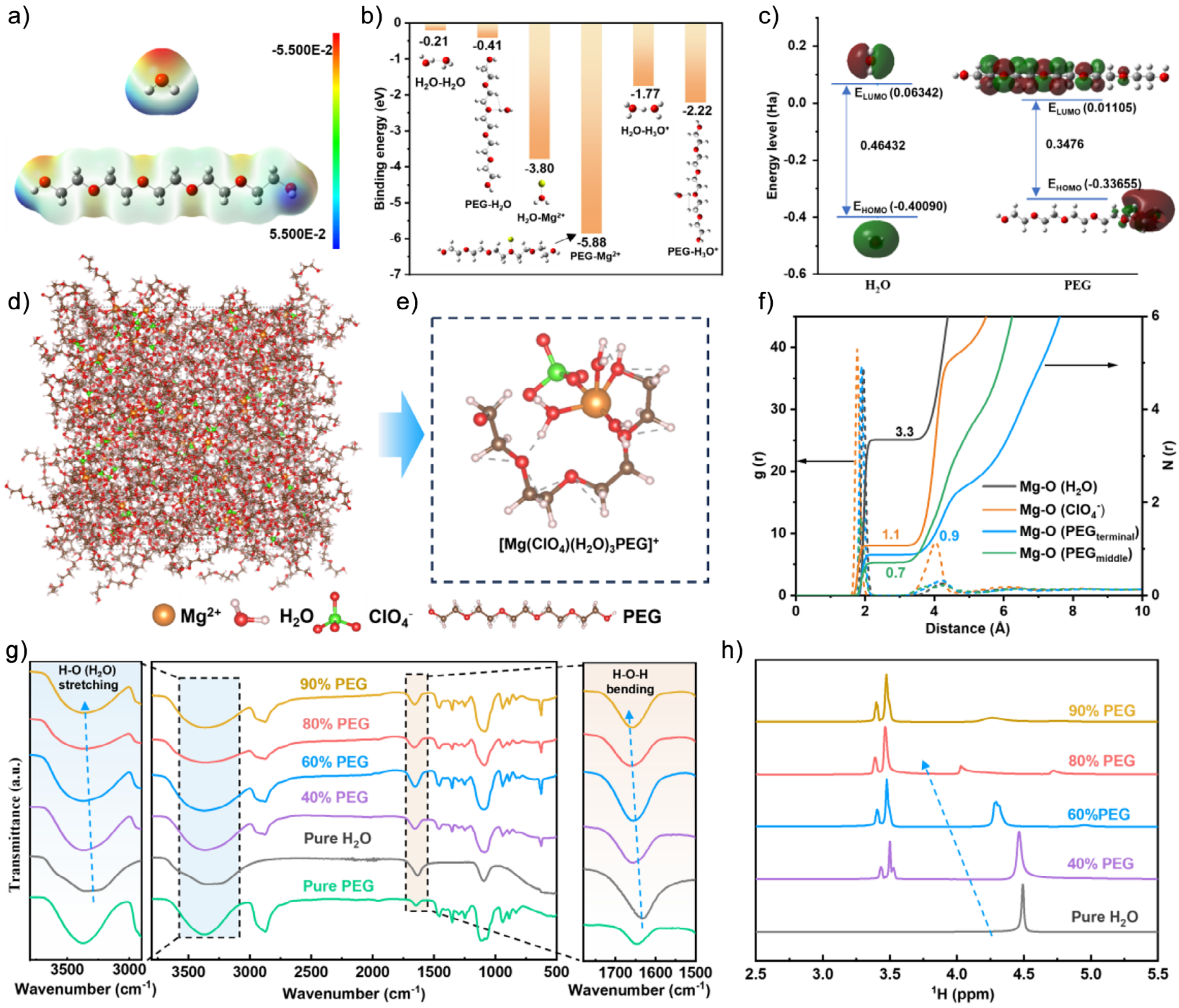

Figure 2. Characterization of electrolyte solvation structure. a) Electrostatic potential mapping of H_2O and PEG. b) Binding energy between PEG, H_2O, and Mg^{2+}. c) LUMO and HOMO energy level of H_2O and PEG d) Snapshot of 1 M $Mg(ClO_4)_2$ in 60% PEG electrolyte. e) The solvated structure of Mg^{2+} ion in 60% PEG electrolyte. f) The RDF of g(r), and coordination number N(r) of Mg -O(ClO_4^-, H_2O, and PEG) in 60% PEG electrolyte. g) FTIR spectroscopy and h) nuclear magnetic resonance (NMR) spectroscopy of the prepared series electrolytes.

(SEM) images reveal that the morphology of NHVO is nanobelts (Figure S10). High -resolution TEM (HRTEM) image of NHVO (Figure 3b) shows clear lattice fringes with the lattice spacing of 8.30 Å corresponds to the (002) crystal planes. Energy-dispersive X-ray (EDX) spectroscopy (Figure S11) confirms the homogeneous distribution of V, O, and N elements. X-ray photoelectron spectroscopy (XPS) analysis (Figure S12) reveals that the vanadium in NHVO is in the +5 oxidation state. Due to the high solubility of vanadium oxides in aqueous electrolytes, we further regulated the electrode structure by constructing a freestanding NHVO/GO/CNT composite electrode. The SEM images of the NHVO/GO/CNT electrode reveal uniform mixing of NHVO, GO, and CNTs, and that the NHVO/GO/CNT electrode has a uniform and relatively dense structure (Figures 3c and S13). The presence of CNTs and GO contribute to enhancing the electronic conductivity of the electrode, while GO also serves to suppress the dissolution of NHVO.[23,24] However, SEM images of the NHVO electrode (Figure S14) prepared by the roll-pressing method show the presence of cracks, a loose and porous structure, and agglomeration of NHVO nanobelts, which could exacerbate the dissolution and structural degradation of NHVO.

Furthermore, coin cells were assembled with various electrodes and electrolytes to assess the impact of electrolytes and electrodes structure on the Mg storage performance of NHVO. Figure 3d compares the rate capability of the NHVO/GO/CNT and NHVO electrodes with different electrolytes. The results indicate that NHVO/GO/CNT exhibits optimal rate performance in 60% PEG electrolyte, delivering discharge capacities of 233.9, 174.5, 161.6, 157.5, 144.4, and 137.5 mAh g^{-1} as the current density increases from 200 to

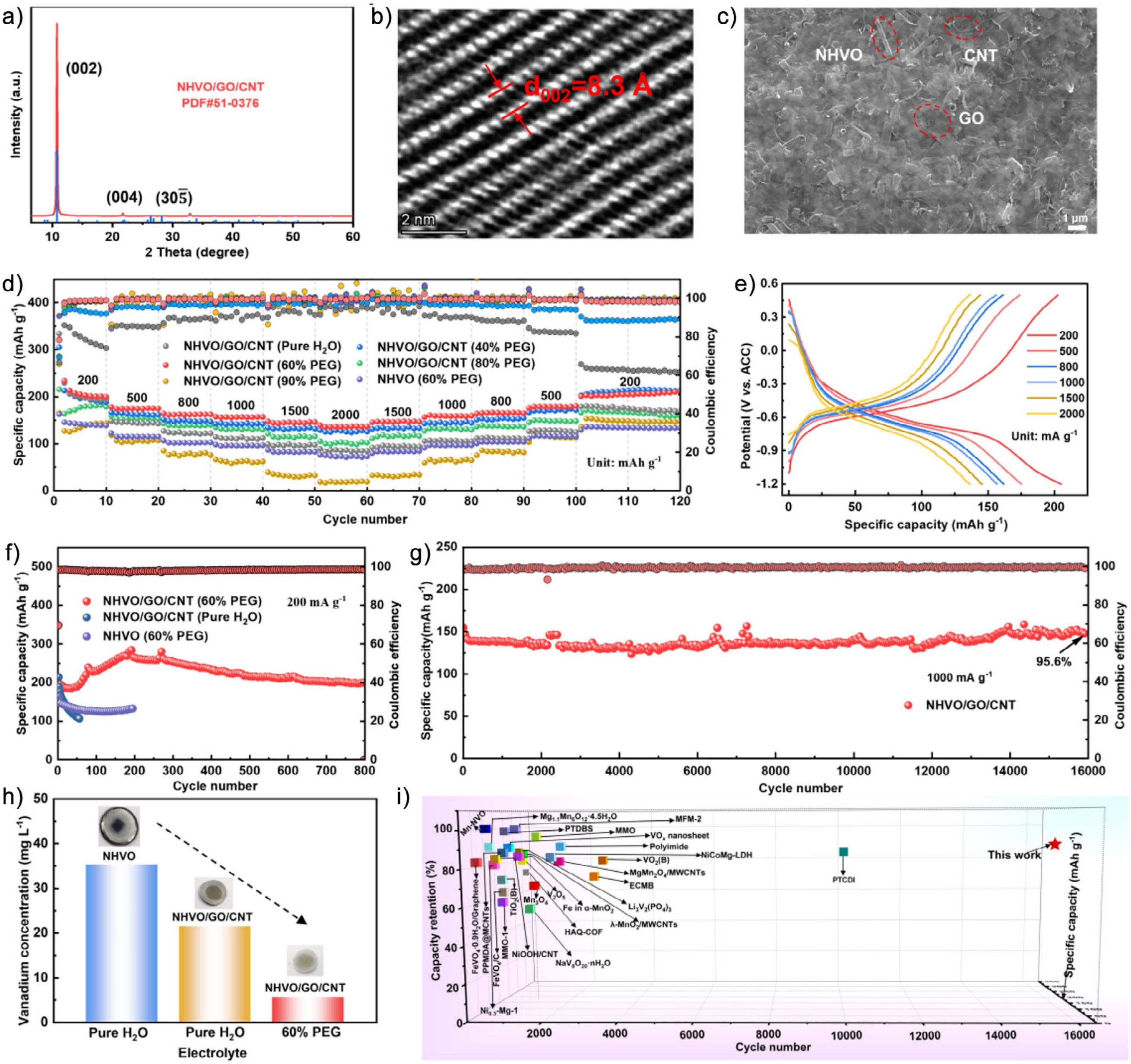

Figure 3. Characterization and electrochemical performances of NHVO/GO/CNT. a) XRD pattern of the NHVO/GO/CNT. b) HRTEM image of NHVO. c) SEM image of NHVO/GO/CNT electrode surface. d) Rate performances of NHVO/GO/CNT and NHVO in different electrolytes. e) The corresponding GCD curves of NHVO/GO/CNT in 60% PEG electrolyte with various current density. f) Cycling performances of NHVO/GO/CNT and NHVO at 200 mA g^{-1}. g) Cycling performances of NHVO/GO/CNT with 60% PEG electrolyte at 1000 mA g^{-1}. h) ICP-OES analysis of separators for NHVO/GO/CNT and NHVO in different electrolytes after 40 cycles (the insert shows the separators after 40 cycles). i) Comparison of the Mg storage performances of NHVO/GO/CNT with reported electrode materials for AMIBs.[9,15,22,26–29,16,30–45,19]

2000 mA g^{-1}, along with a Coulombic efficiency (CE) exceeding 98%. The corresponding galvanostatic charge-discharge (GCD) curves (Figure 3e) indicate that NHVO/GO/CNT electrode has a stable voltage profile at different current densities. In contrast, NHVO/GO/CNT, in pure H_2O electrolyte, demonstrates the lowest Coulombic efficiency (below 70% at 200 mA g^{-1}), likely due to the poor stability of the pure H_2O electrolyte. In 90% PEG electrolyte, NHVO/GO/CNT shows the worst rate performance (only 18.4 mAh g^{-1} at 2000 mA g^{-1}), which is attributed to the poor ionic conductivity of the 90% PEG electrolyte. Although NHVO/GO/CNT in 40% PEG electrolyte exhibits rate discharge capacities comparable to those in 60% PEG electrolyte, its CE at low current densities is inferior. Therefore, the 60% PEG electrolyte is expected to achieve a balance between rate performance and cycling stability for NHVO/GO/CNT electrode. Furthermore, a comparison with the rate performance of NHVO electrode in 60% PEG electrolyte confirms that electrode structure regulation can effectively enhance the electronic conductivity of NHVO/GO/CNT. Figure 3f compares the cycling performance of NHVO/GO/CNT and NHVO electrodes at the low current density of 200 mA g^{-1} with 60% PEG and pure H_2O electrolytes. In 60% PEG electrolyte, NHVO/GO/CNT presents a capacity retention of 90.8% after 800 cycles and achieves a high Mg storage capacity of 284.0 mAh g^{-1}. The TEM images of NHVO/GO/CNT after 100 cycles (Figure S15), along with the electrochemical impedance spectra (EIS) at various cycling stages (Figure S16), indicate that the activation process may be attributed to the fragmentation of NHVO nanobelts and a decrease in interfacial charge transfer resistance. Moreover, the initial increase in capacity observed during cycling is likely closely associated with the ion exchange between Mg^{2+} and NH_4^+ ions,[23,25] which will be further elaborated in a subsequent section. However, NHVO/GO/CNT in pure H_2O electrolyte and NHVO in 60% PEG electrolyte both exhibit rapid capacity fading and lower specific capacity, further underscoring the critical importance of the synergistic regulation of electrolyte and electrode structure in enhancing the electrochemical performance of electrode materials. Remarkably, NHVO/GO/CNT in 60% PEG electrolyte achieves 95.6% capacity retention after 16000 cycles at 1000 mA g^{-1} (Figure 3g), demonstrating exceptional long-term stability. The cyclic voltammetry (CV) curve of NHVO/GO/CNT in 60% PEG electrolyte is shown in Figure S17a and the redox peaks align well with the charge/discharge plateaus observed in the GCD curve (Figure S17b). Moreover, inductively coupled plasma optical emission spectroscopy (ICP-OES) analysis of separators for NHVO/GO/CNT in both 60% PEG and pure H_2O electrolytes, as well as for NHVO in 60% PEG electrolyte (Figure 3h), confirms that the synergistic regulation strategy effectively suppresses vanadium dissolution. Finally, compared with the reported electrode materials in AMIBs (Figure 3i and Table S1), NHVO/GO/CNT exhibits the longest life of 16000 cycles with an impressive 95.6% capacity retention in 60% PEG electrolyte. These results collectively demonstrate that the synergistic regulation of electrode and electrolyte structure effectively enhances the electrochemical performance of AMIBs.

To demonstrate the Mg storage mechanism of NHVO/GO/CNT in 60% PEG electrolyte, a suite of advanced characterization techniques was employed, including In situ XRD, in situ attenuated total reflection Fourier-transform infrared (ATR–FTIR), ex situ XPS and ex situ time-of-flight secondary ion mass spectrometry (TOF-SIMS). Figure 4a illustrates the configuration of the in situ ATR–FTIR testing cell. The spectra in Figure 4b reveals periodic intensity variations of absorption bands, demonstrating reversible electrochemical processes of NHVO/GO/CNT electrode. The weakened characteristic peaks of ClO_4^- at 1050–1100 cm^{-1} during discharge, attributed to ClO_4^- migration toward the anode, with the reverse trend observed during charging. The reversible change in the intensity of the PEG absorption peak ($-CH_3$ and $-CH_2$) is due to the desolvation and resolvation of Mg^{2+} ions during discharging and charging. And during discharging, the absorption band of the $V = O$ stretching, attributed to the $[VO_6]$ octahedron, exhibits a red-shift and gradually increases in intensity. This is caused by the reduction of V^{5+} as a result of Mg^{2+} insertion.[46] During the subsequent charging process, the absorption peak shows the opposite behavior, with a decrease in intensity and a blue-shift, which confirms the reversible nature of the Mg^{2+} insertion/deinsertion processes. The reversible evolution of V=O absorption bands further confirm the structural reversibility of NHVO/GO/CNT. The dynamic behavior of the 60% PEG electrolyte during charging and discharging is shown in Figure S18. Upon discharging, ClO_4^- ions migrate to the anode, and Mg^{2+} ions shed their solvent shells before inserting into the NHVO/GO/CNT. The charging process involves the exact opposite movements. Figure 4c displays the in situ XRD patterns and corresponding GCD curves during the first two cycles. During the initial discharge, the (002), (004), and (305) diffraction peaks of NHVO/GO/CNT shift to higher angles, indicating lattice contraction along the *a*- and *c*-axes because of enhanced interlayer interactions induced by Mg^{2+} insertion. As the amount of inserted Mg^{2+} increases, the positions of the three diffraction peaks remain essentially unchanged. This could be attributed to the exchange between Mg^{2+} and NH_4^+. Since one Mg^{2+} ion can replace two NH_4^+ ions, the interlayer interaction does not strengthen with the increasing insertion of Mg^{2+}. This ion exchange phenomenon will be further discussed in the ex situ characterization section. Upon charging, all peaks return to their original positions, and reversible redox behavior is maintained in subsequent cycles, confirming the excellent structural reversibility of NHVO/GO/CNT in 60% PEG electrolyte. The in situ XRD results demonstrates that the Mg storage mechanism of NHVO/GO/CNT is a single-phase solid solution reaction. The evolution observed in the ex situ XRD patterns (Figure S19) is consistent with that seen in the in situ XRD result. The Mg 1s XPS spectra of NHVO/GO/CNT at different states show that the peak intensity increases during discharge and decreases during charge (Figure 4d), corresponding to an increase and subsequent decrease in Mg content (Figure S20). Depth-dependent Mg 1s XPS profiles of the discharged ang charged NHVO/GO/CNT (Figure S21) and quantitative analysis further corroborate reversible Mg^{2+} ions storage. However, even after 120 s of Ar^+ ion etching, the Mg 1s peak was still observed in the XPS spectrum of the fully charged NHVO/GO/CNT (Figure S21c), which may be due to the displacement of Mg^{2+} by NH_4^+. The absence of N element in the depth etching analysis of the N 1s spectrum of the fully discharged NHVO/GO/CNT further indicates that NH_4^+ is displaced by Mg^{2+} (Figure S22). Since the charge of Mg^{2+} ions is twice compared to that of NH_4^+ ions, one Mg^{2+} can replace two NH_4^+ ions, which is beneficial to releasing more Mg^{2+} storage sites. In addition, the ion exchange phenomenon may lead to the formation of metastable vanadium oxides, which are more favorable for multivalent ion storage.[25] Therefore, the capacity increase observed in Figure 3f might be closely related to the ion displacement phenomenon.[23] The ex situ XPS spectra of V 2p indicate that V^{5+} is reduced to V^{4+} during Mg^{2+} insertion, and a reversible change in valence state is observed during the charging process (Figure 4e). And reversible V valence changes are also visually supported by color variations of the NHVO/GO/CNT electrode at different states (Figure S23). The TOF-SIMS 3D reconstruction images and the surface

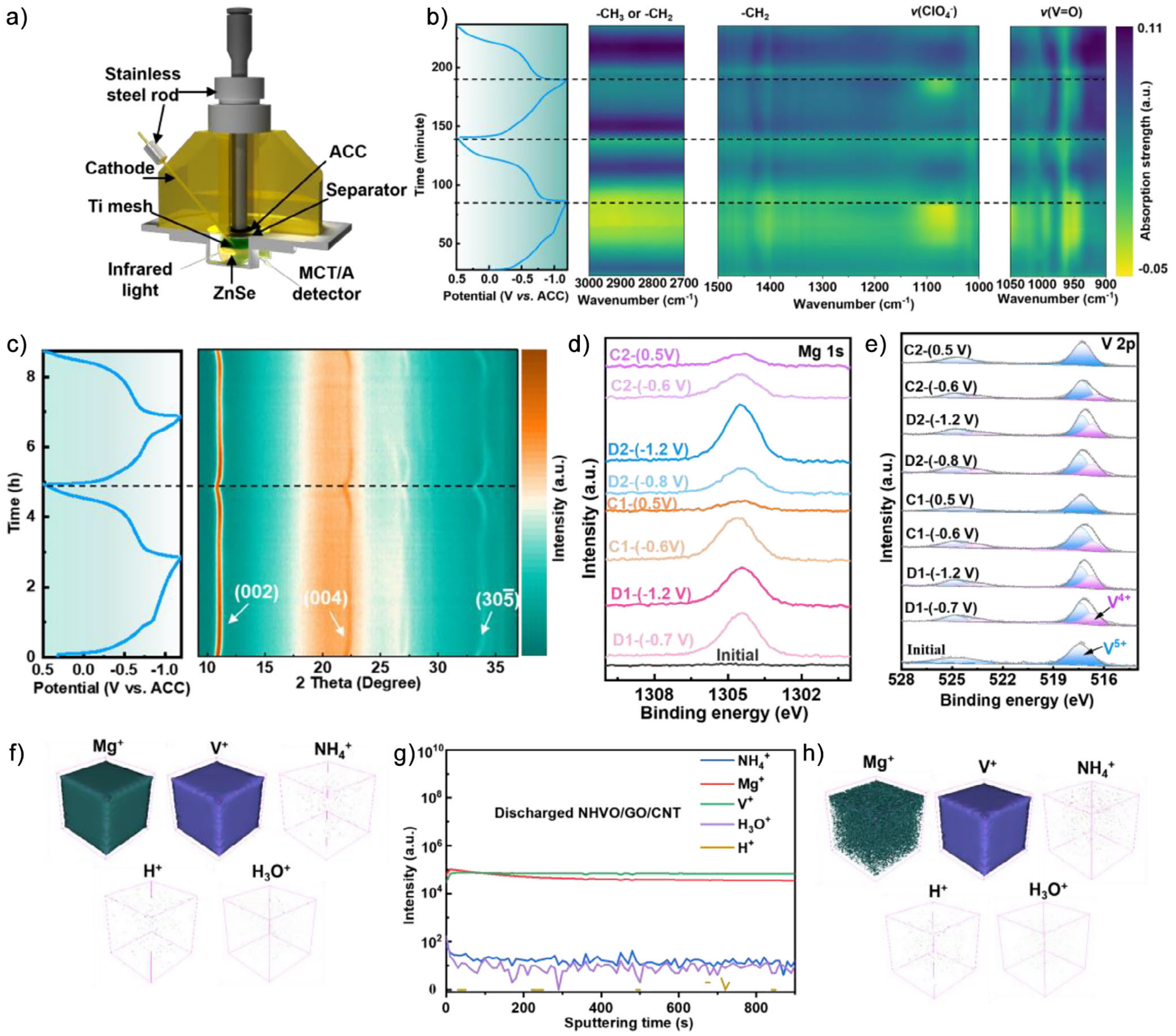

Figure 4. The energy storage mechanism of NHVO/GO/CNT electrode with 60% electrolyte. a) The configuration of the cell for in situ ATR–FTIR tests. b) In situ FTIR result. c) In situ XRD result. The XPS results of d) Mg 1s and e) V 2p of NHVO/GO/CNT electrode at different states of charge/discharge. f) TOF -SIMS 3D images and g) the depth profiles of the discharged NHVO/GO/CNT at the 5th cycle. h) TOF-SIMS 3D images of the charged NHVO/GO/CNT at the 5th cycle.

ions images of the fully discharged NHVO/GO/CNT at 5th cycle (Figures 4f and S24) reveal homogeneous distributions of Mg^+ and V^+ fragments, while signals for NH_4^+, H^+, and H_3O^+ are nearly absent. The absence of H^+ and H_3O^+ suggests that H^+ or H_3O^+ may not be inserted into NHVO during discharging. The content of Ca^+ and V^+ remains constant even after 900 s sputtering, and the content of NH_4^+, H^+, and H_3O^+ is very low (Figure 4g). The TOF-SIMS of the charged NHVO/GO/CNT (Figures 4h, S25, and S26) reveals a weak Mg^+ signal, which is attributed to the displacement of NH_4^+ by Mg^{2+}. Combined with the N 1s XPS depth profile of the discharged state NHVO/GO/CNT (Figure S22), the results further confirm that the NH_4^+ ions are not reinserted into NHVO/GO/CNT during discharging and the capacity contribution is primarily attributed to the insertion of Mg^{2+} ions. The above results confirm that the NHVO/GO/CNT exhibits excellent structural reversibility in the 60% PEG electrolyte.

DFT calculations were performed to gain a deeper understanding of the behavior of molecular crowding electrolytes at the electrode interface and the mechanism of inhibiting vanadium oxide dissolution. DFT calculations revealed that PEG exhibits a higher adsorption energy compared to H_2O molecules on the NHVO surface (Figure 5a). This suggests that PEG preferentially adsorbs on the material surface to form a spatial barrier, thereby inhibiting the outward diffusion of dissolved V-based ions. Additionally, the energy barriers for removing V atoms from the NHVO structure in pure H_2O and molecular crowding electrolytes were calculated (Figure 5b). The results revealed that the dissolution of V

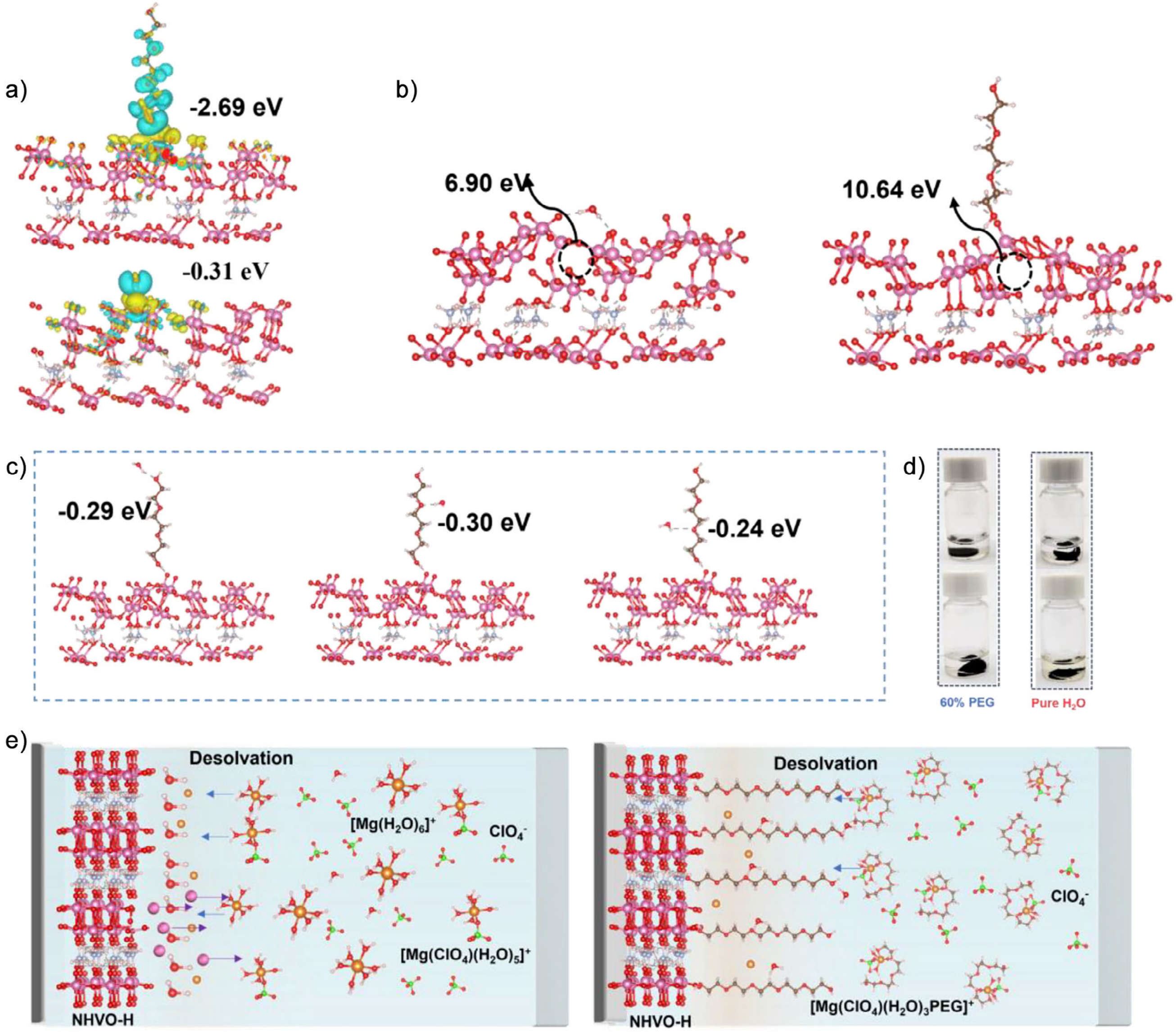

Figure 5. Mechanisms of interface adsorption regulation for molecular crowding electrolytes. a) The calculated adsorption energies of H_2O and PEG molecules on NHVO surface. b) The energy barrier for removing V atom from NHVO in pure H_2O and 60% PEG electrolytes. c) The binding energy between H_2O and PEG adsorbed on NHVO surface. d) Optical photographs of the NHVO/GO/CNT electrodes after immersion in pure H_2O and 60% PEG electrolytes for a duration of three days, respectively. e) Schematic illustration of the interface adsorption regulation in PEG molecular crowding and pure H_2O electrolytes, and a corresponding mechanism for suppressing V dissolution.

was more challenging in PEG molecular crowding electrolyte, validating the previous deduction. Furthermore, we observed that the O atoms or terminal hydroxyl (-OH) groups of PEG molecules adsorbed on NHVO can interact with H_2O molecules in the electrolyte (Figure 5c), forming a spatial barrier that prevents the accumulation of reactive H_2O molecules on the electrode surface. This effectively suppresses vanadium dissolution during electrochemical processes. Moreover, immersion experiments (Figure 5d) showed that NHVO/GO/CNT remained stable in the 60% PEG electrolyte but dissolved in the pure H_2O electrolyte, reconfirming that PEG can mitigate the dissolution of NHVO to some extent. The DFT calculation results further indicate that the PEG molecular crowding agent not only broadens the ESW of electrolytes but also, to some extent, inhibits the dissolution of vanadium oxides. These findings corroborate the conclusions presented in Figure 3h. Finally, Figure 5e summarizes the interfacial mechanism in both molecular crowding electrolyte and pure H_2O electrolyte. In the molecular crowding electrolyte, PEG molecules can be adsorbed on the NHVO surface, effectively suppressing the attack of active H_2O molecules on NHVO and inhibiting vanadium dissolution. Conversely, in pure H_2O electrolyte, H_2O molecules accumulate on the NHVO surface, readily leading to structural damage and vanadium dissolution, which results in the electrode material exhibiting poor cycling performance.

To further validate the practical applicability of the synergistic regulation strategy in full cells, a NiHCF cathode

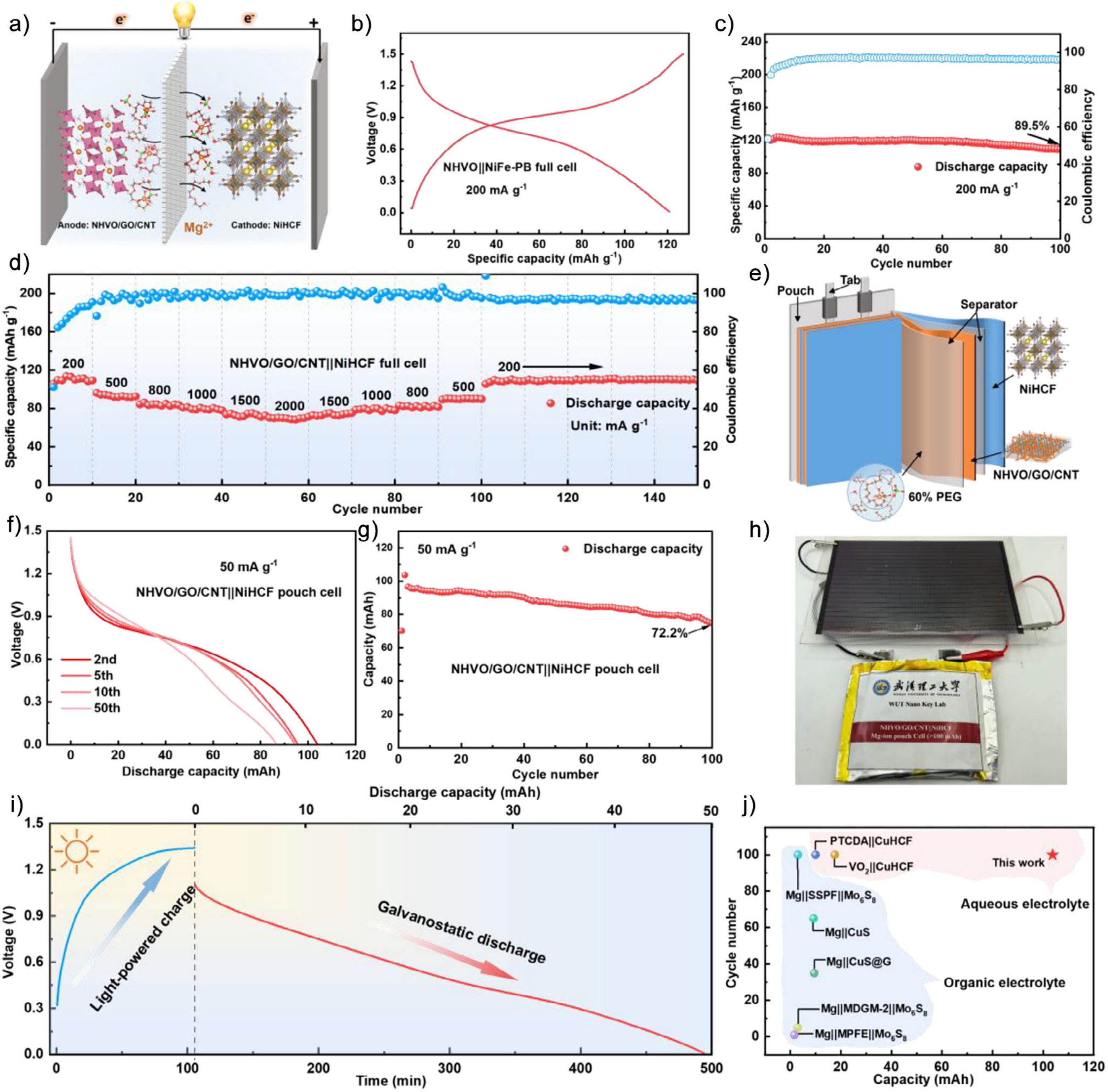

Figure 6. Electrochemical performance of NHVO/GO/CNT||NiHCF full cell. a) Schematic diagram of NHVO/GO/CNT||NiHCF full cell. b) GCD curve and c) cycling performance at 200 mA g^{-1}. d) Rate performance. e) Schematic diagram of a multilayer aqueous Mg-ion pouch cell. f) The discharge curves and g) cycling performance of the multilayer pouch cell at 50 mA g^{-1}. h) Photo of the integrated solar cell-pouch cell device. i) Light-powered charging curve and the galvanostatic discharge curve of the multilayer pouch cell at 10 mA g^{-1}. j) Comparison of the performances of the multilayer aqueous Mg-ion pouch cell with the reported aqueous and nonaqueous Mg-ion pouch cells. [5–7,16,48–52]

material was synthesized to assemble an aqueous Mg-ion full cells. The XRD pattern confirms the successful preparation of the NiHCF cathode material (Figure S27).[47] SEM image and elemental mappings of NiHCF powder (Figure S28) show the homogeneous distribution of Na, Ni, Fe, C, and N. To verify the compatibility of NiHCF with the 60% PEG electrolyte, the electrochemical performance of NiHCF was evaluated. The CV curves in Figure S29a exhibit highly reversible redox peaks, corresponding to the voltage plateaus in the GCD curves shown in Figure S29b. The cycling performance in Figure S29c demonstrates excellent stability, with 98% capacity retention after 1300 cycles. Subsequently, we assembled a NHVO/GO/CNT||NiHCF full cell (Figure 6a) using NiHCF cathode, 60% PEG electrolyte, and NHVO/GO/CNT anode. The full cell has a discharge specific capacity of 120.9 mAh g^{-1} (Figure 6b) and maintains 89.5% capacity retention after 100 cycles (Figure 6c) at 200 mA g^{-1}. As shown in Figures 6d and S30, the full cell exhibits the specific capacity of 113.8, 96.2, 86.2, 81.5, 74.8, and 70.2 mAh g^{-1} at 200, 500, 800, 1000, 1500, and 2,000 mA g^{-1}, respectively. Moreover, stable cycling and reversible capacity are maintained when reverting to 200 mA g^{-1}. To further illustrate the practical potential of this full cell, a multilayer aqueous Mg-ion pouch cell was assembled, and the schematic diagram of the assembled multilayer pouch cell is presented in Figures 6e and S31. The multilayer pouch cell delivers the highest capacity of 103.7 mAh (Figure 6f) and a capacity retention of 72.2% after 100 cycles (Figure 6g). The corresponding gravimetric discharge curves are shown in Figure S32. Subsequently, the integrated solar cell-pouch cell device (Figure 6h) demonstrated, for the first time, the feasibility of photo-charging AMIBs. After being charged by a solar cell for 105 min (Figure S33), the multilayer pouch cell could sustain a constant current discharge for 385 min (corresponding to a capacity of 46 mAh) (Figure 6i). The results indicate the potential for this aqueous Mg-ion pouch cell to integrate with renewable energy sources like solar power, making it a promising candidate for large-scale energy storage applications. Finally, compared with reported aqueous and nonaqueous Mg -ion pouch cells to date (Figure 6j), the assembled NHVO/GO/CNT||NiHCF multilayer pouch cell exhibits the highest capacity among all systems and long cycle life (Table S2).

Although considerable progress has been made in developing high-performance AMIBs, key challenges remain, including low operating voltage and gas evolution under high-temperature conditions. To overcome these issues, developing semi-solid-state polymer-based electrolytes with good thermal stability and a wider electrochemical stability window may represent a promising future direction. Recently, various types of polymer-based Mg electrolytes[53,54] have been reported for use in organic Mg batteries, demonstrating considerable application potential. However, the relatively low ionic conductivity of semi-solid polymer-based electrolytes may diminish the exceptional rate performance of AMIBs. Therefore, achieving a balance between rate capability, high-temperature performance, and working voltage is essential for the successful application of semi-solid polymer-based electrolytes in AMIBs.

Conclusion

In summary, this work reports a synergistic regulation strategy of electrode and electrolyte structure for high-performance AMIBs. Regarding electrolyte regulation, the addition of PEG molecular crowding agent can not only modulate the solvation structure of electrolyte to widen the ESW, but also forms a spatial barrier on the electrode surface to inhibit the dissolution of vanadium oxides. For electrode structure regulation, the constructed freestanding NHVO/GO/CNT composite electrode has higher electron conductivity while inhibiting the dissolution and structural degradation of NHVO. Under the effect of the synergistic regulation, the NHVO/GO/CNT delivers a 284 mAh g^{-1} high discharge capacity and the longest cycling lifespan of 16000 cycles with a 95.6% high capacity retention after at 1000 mA g^{-1}. The Mg-storage mechanism of NHVO based on a single-phase insertion/extraction reaction, and the displacement phenomenon between Mg^{2+} and NH_4^+ were revealed by various advanced in situ/ex situ characterization techniques. The assembled NHVO/GO/CNT||NIHCF full cell exhibits a discharge capacity of 120.9 mAh g^{-1} at 200 mA g^{-1}. And the assembled multilayer aqueous Mg-ion pouch cell delivers the highest capacity of 103.7 mAh among all reported Mg-ion pouch cells. Furthermore, the integrated solar cell-pouch cell device demonstrates the feasibility of photo-charging AMIBs for the first time. Consequently, this work provides a novel strategy for improving the performance of AMIBs and shows great promise for advancing the development of practical AMIBs.

Acknowledgements

This work was supported by the National Key Research and Development Program of China (2023YFB3809500), the Postdoctoral Fellowship Program of CPSF under Grant Number (GZB20250033), the National Natural Science Foundation of China (52472246), the Natural Science Foundation of Hubei Province (2022CFA087).

Conflict of Interests

The authors declare no conflict of interest.

Data Availability Statement

The data that support the findings of this study are available from the corresponding author upon reasonable request.

Keywords: Aqueous magnesium-ion batteries • Mg-ion pouch cells • Molecular crowding electrolyte • Multivalent-ion batteries • Vanadium oxides

---

[1] Y. Liang, H. Dong, D. Aurbach, Y. Yao, *Nat. Energy* **2020**, *5*, 646–656.
[2] R. Li, L. Tong, Y. Jiang, Y. Wang, J. Long, X. Chen, J. Wu, X. Li, Y. Chen, *Interdiscip. Mater.* **2024**, *3*, 150–159.
[3] J. Wang, R. Yu, J. Wang, J. Long, F. Qiao, L. Zhang, G. He, Q. An, L. Mai, *J. Magnes. Alloys.* **2023**, *11*, 4181–4188.
[4] H. D. Yoo, I. Shterenberg, Y. Gofer, G. Gershinsky, N. Pour, D. Aurbach, *Energy Environ. Sci.* **2013**, *6*, 2265–2279.
[5] Q. Su, W. Wang, J. Chen, J. Ji, W. Wang, W. Ren, L. Zhang, J. Xie, Q. An, *Adv. Funct. Mater.* **2024**, *35*, 2419594.
[6] J. Long, S. Tan, J. Wang, F. Xiong, L. Cui, Q. An, L. Mai, *Angew. Chem. Int. Ed.* **2023**, *62*, e202301934.
[7] J. Wang, S. Tan, G. Zhang, Y. Jiang, Y. Yin, F. Xiong, Q. Li, D. Huang, Q. Zhang, L. Gu, Q. An, L. Mai, *Sci China Mater.* **2020**, *63*, 1651–1662.
[8] C. Yuan, Y. Zhang, Y. Pan, X. Liu, G. Wang, D. Cao, *Electrochim. Acta.* **2014**, *116*, 404–412.
[9] F. Wang, X. Fan, T. Gao, W. Sun, Z. Ma, C. Yang, F. Han, K. Xu, C. Wang, *ACS Cent. Sci.* **2017**, *3*, 1121–1128.
[10] J. A. Blázquez, R. R. Maça, O. Leonet, E. Azaceta, A. Mukherjee, Z. Zhao-Karger, Z. Li, A. Kovalevsky, A. Fernández-Barquín, A. R. Mainar, P. Jankowski, L. Rademacher, S. Dey, S. E. Dutton, C. P. Grey, J. Drews, J.

Häcker, T. Danner, A. Latz, D. Sotta, M. R. Palacin, J.-F. Martin, J. M. G. Lastra, M. Fichtner, S. Kundu, A. Kraytsberg, Y. Ein-Eli, M. Noked, D. Aurbach, *Energy Environ. Sci.* **2023**, *16*, 1964–1981.

[11] X. Song, Y. Ge, H. Xu, S. Bao, L. Wang, X. Xue, Q. Yu, Y. Xing, Z. Wu, K. Xie, T. Zhu, P. Zhang, Y. Liu, Z. Wang, Z. Tie, J. Ma, Z. Jin, *J Am Chem Soc.* **2024**, *146*, 7018–7028.

[12] Y. P. Zhu, X. R. Guo, Y. J. Lei, W. X. Wang, A. H. Emwas, Y. Y. Yuan, Y. He, H. N. Alshareef, *Energy Environ. Sci.* **2022**, *15*, 1282–1292.

[13] Q. Fu, X. Wu, X. Luo, Z. Ding, S. Indris, A. Sarapulova, Z. Meng, M. Desmau, Z. Wang, W. Hua, C. Kübel, B. Schwarz, M. Knapp, H. Ehrenberg, Y. Wei, S. Dsoke, *Energy Storage Mater.* **2024**, *66*, 103212.

[14] Q. Fu, X. Y. Wu, X. L. Luo, S. Indris, A. Sarapulova, M. Bauer, Z. Q. Wang, M. Knapp, H. Ehrenberg, Y. J. Wei, S. Dsoke, *Adv. Funct. Mater.* **2022**, *32*, 2110674.

[15] X. Wang, X. Zhang, G. Zhao, H. Hong, Z. Tang, X. Xu, H. Li, C. Zhi, C. Han, *ACS Nano.* **2022**, *16*, 6093–6102.

[16] M. Huang, X. Wang, J. Wang, J. Meng, X. Liu, Q. He, L. Geng, Q. An, J. Yang, L. Mai, *Angew. Chem. Int. Ed.* **2023**, *62*, e202308961.

[17] S. Zhang, Y. Wang, Y. Sun, Y. Wang, Y. Yang, P. Zhang, X. Lv, J. Wang, H. Zhu, Y. NuLi, *Small.* **2023**, *19*, e2300148.

[18] M. Wang, S. Yagi, *J. Alloys Compd.* **2020**, *820*, 153135.

[19] Z. Pan, Z. Jiang, T. Qin, D. Wang, F. Liu, H. Yang, Q. Liang, W. Zhang, W. Zheng, *Angew. Chem. Int. Ed.* **2025**, *64*, e202503535.

[20] H. Y. Zhang, D. X. Cao, X. Bai, *Inorganic Chem. Front.* **2020**, *7*, 2168–2177.

[21] W. Zhang, S. Zhu, T. Yang, L. Wu, J. Li, J. Liang, Y. Liu, L. Cui, C. Tang, X. Chen, H. Zhou, F. Qiao, M. Zhou, P. Luo, F. Chi, X. Liao, L. Zhang, Q. An, *Angew. Chem. Int. Ed.* **2025**, *64*, e202419732.

[22] Q. Fu, X. Wu, X. Luo, S. Indris, A. Sarapulova, M. Bauer, Z. Wang, M. Knapp, H. Ehrenberg, Y. Wei, S. Dsoke, *Adv. Funct. Mater.* **2022**, *32*, 2110674.

[23] J. Wang, Y. Zhang, F. Qiao, Y. Jiang, R. Yu, J. Li, S. Lee, Y. Dai, F. Guo, P. Jiang, L. Zhang, Q. An, G. He, L. Mai, *Adv. Mater.* **2024**, *36*, 2403371.

[24] H. Dong, O. Tutusaus, Y. L. Liang, Y. Zhang, Z. Lebens-Higgins, W. L. Yang, R. Mohtadi, Y. Yao, *Nature Energy.* **2020**, *5*, 1043–1050.

[25] J. L. Andrews, A. Mukherjee, H. D. Yoo, A. Parija, P. M. Marley, S. Fakra, D. Prendergast, J. Cabana, R. F. Klie, S. Banerjee, *Chem.* **2018**, *4*, 564–585.

[26] L. Chen, J. L. Bao, X. Dong, D. G. Truhlar, Y. Wang, C. Wang, Y. Xia, *ACS Energy Lett.* **2017**, *2*, 1115–1121.

[27] Z. Fu, H. Zhang, D. Geng, Z. Liu, Z. Zhang, X. Li, C. Yan, *Adv. Energy Mater.* **2024**, *15*, 2403934.

[28] G. Zou, Z. Tian, V. S. Kale, W. Wang, S. Kandembeth, Z. Cao, J. Guo, J. Czaban-Jóźwiak, L. Cavallo, O. Shekhah, M. Eddaoudi, H. N. Alshareef, *Adv. Energy Mater.* **2022**, *13*, 2203193.

[29] W. Kou, Z. Fang, H. Ding, W. Luo, C. Liu, L. Peng, X. Guo, W. Ding, W. Hou, *Adv. Funct. Mater.* **2024**, *34*, 2406423.

[30] B. Wen, C. Yang, J. Wu, J. Liu, W. Wang, J. Yang, X. Chi, Y. Liu, *Chem. Eng. J.* **2022**, *435*.

[31] Y. Zhang, G. Liu, C. Zhang, Q. Chi, T. Zhang, Y. Feng, K. Zhu, Y. Zhang, Q. Chen, D. Cao, *Chem. Eng. J.* **2020**, *392*.

[32] H. Zhang, K. Ye, K. Zhu, R. Cang, J. Yan, K. Cheng, G. Wang, D. Cao, *Chem. Eur. J.* **2017**, *23*, 17118–17126.

[33] H. Zhang, K. Ye, K. Zhu, R. Cang, J. Yan, K. Cheng, G. Wang, D. Cao, *Electrochim. Acta.* **2017**, *256*, 357–364.

[34] C. Sun, G. Huang, C. Xu, L. Li, A. Tang, X. Zhou, J. Wang, F. Pan, *Energy Storage Mater.* **2024**, *66*.

[35] B. He, Y. Ling, Z. Wang, W. Gong, Z. Wang, Y. Liu, T. Zhou, T. Xiong, S. Wang, Y. Wang, Q. Li, Q. Zhang, L. Wei, *eScience.* **2024**, *4*, 100293.

[36] H. Zhang, D. Cao, X. Bai, *Inorg. Chem. Front.* **2020**, *7*, 2168–2177.

[37] Y. Zhao, B. Wang, M. Shi, S. An, L. Zhao, C. Yan, *Int. J. Miner. Metall. Mater.* **2022**, *29*, 1954–1962.

[38] D. Zhang, D. Li, J. Zhang, T. Sun, *J. Electroanal. Chem.* **2021**, *901*, 115764.

[39] Y. Tian, N. Liu, T. A. Otitoju, Y. Wang, Z. Feng, T. Sun, *J. Energy Storage.* **2023**, *72*, 108357.

[40] C. Sun, H. Wang, F. Yang, A. Tang, G. Huang, L. Li, Z. Wang, B. Qu, C. Xu, S. Tan, X. Zhou, J. Wang, F. Pan, *J. Magnes. Alloys* **2023**, *11*, 840–850.

[41] Q. Wang, Z. Liu, T. Xu, H. Li, Y. Chen, Y. Yan, *J. Power Sources.* **2024**, *611*, 234763.

[42] H. Zhang, K. Ye, X. Huang, X. Wang, K. Cheng, X. Xiao, G. Wang, D. Cao, *J. Power Sources.* **2017**, *338*, 136–144.

[43] X. Song, Y. Ge, H. Xu, S. Bao, L. Wang, X. Xue, Q. Yu, Y. Xing, Z. Wu, K. Xie, T. Zhu, P. Zhang, Y. Liu, Z. Wang, Z. Tie, J. Ma, Z. Jin, *J. Am. Chem. Soc.* **2024**, *146*, 7018–7028.

[44] Z. Shi, L. Xue, J. Wu, Q. Guo, Q. Xia, M. Ni, P. Wang, S. V. Savilov, S. M. Aldoshin, F. Zan, H. Xia, *J. Electrochem. Soc.* **2021**, *168*, 120549.

[45] D. Zhang, D. Du, J. Zhang, Z. Feng, T. Sun, *J. Electrochem. Soc.* **2022**, *169*, 040530.

[46] Q. Wei, J. Liu, W. Feng, J. Sheng, X. Tian, L. He, Q. An, L. Mai, *J. Mater. Chem. A* **2015**, *3*, 8070.

[47] J. Peng, M. Ou, H. Yi, X. Sun, Y. Zhang, B. Zhang, Y. Ding, F. Wang, S. Gu, C. A. López, W. Zhang, Y. Liu, J. Fang, P. Wei, Y. Li, L. Miao, J. Jiang, C. Fang, Q. Li, M. T. Fernández-Díaz, J. A. Alonso, S. Chou, J. Han, *Energy Environ. Sci.* **2021**, *14*, 3130–3140.

[48] Y. Du, Y. Chen, S. Tan, J. Chen, X. Huang, L. Cui, J. Long, Z. Wang, X. Yao, B. Shang, G. Huang, X. Zhou, L. Li, J. Wang, F. Pan, *Energy Storage Mater.* **2023**, *62*, 102939.

[49] P. Liu, J. Long, R. Wang, Y. Zhou, B. Qu, L. Zhang, X. Zhou, Q. An, *Energy Storage Mater.* **2024**, *71*, 103679.

[50] Y. Zhu, X. Guo, Y. Lei, W. Wang, A.-H. Emwas, Y. Yuan, Y. He, H. N. Alshareef, *Energy Environ. Sci.* **2022**, *15*, 1282–1292.

[51] X. Ge, F. Song, A. Du, Y. Zhang, B. Xie, L. Huang, J. Zhao, S. Dong, X. Zhou, G. Cui, *Adv. Energy Mater.* **2022**, *12*, 2201464.

[52] S. Li, J. Zhang, S. Zhang, Q. Liu, H. Cheng, L. Fan, W. Zhang, X. Wang, Q. Wu, Y. Lu, *Nature Energy.* **2024**, *9*, 285–297.

[53] A. Sarkar, S-Y Huang, V. R. Dharmaraj, B. Bazri, K. Iputera, H-H Su, Y-A Chen, H-C Chen, Y-P Lin, R-J Chung, D-H Wei, R-S Liu, *J. Mater. Chem A.* **2024**, *12*, 25968–25978.

[54] Y. Sun, M. Pan, Y. Wang, A. Hu, Q. Zhou, D. Zhang, S. Zhang, Y. Zhao, Y. Wang, S. Chen, M. Zhou, Y. Chen, J. Yang, J. Wang, Y. NuLi, *Angew. Chem. Int. Ed.* **2024**, *136*, e202406585.

Manuscript received: July 02, 2025
Revised manuscript received: August 06, 2025
Accepted manuscript online: August 11, 2025
Version of record online: ■■, ■■